Fatigue behavior and modeling of additively manufactured IN718: The effect of surface treatments and surface measurement techniques

Seungjong Lee (Conceptualization) (Methodology) (Software) (Validation) (Formal analysis) (Investigation) (Data curation) (Writing – original draft) (Visualization), Shuai Shao (Conceptualization) (Methodology) (Validation) (Investigation) (Formal analysis) (Writing – review and editing) (Visualization) (Supervision), Douglas N. Wells (Conceptualization) (Methodology) (Validation) (Resources) (Writing – review and editing) (Funding acquisition), Miroslav Zetek (Conceptualization) (Methodology) (Validation) (Resources) (Writing – review and editing) (Funding acquisition), Miloslav Kepka (Conceptualization) (Methodology) (Validation) (Resources) (Writing – review and editing) (Funding acquisition), Nima Shamsaei (Conceptualization) (Methodology) (Resources) (Validation) (Formal analysis) (Investigation) (Writing – review and editing) (Supervision) (Project administration) (Funding acquisition)

PII:	S0924-0136(21)00435-0
DOI:	https://doi.org/10.1016/j.jmatprotec.2021.117475
Reference:	PROTEC 117475
To appear in:	*Journal of Materials Processing Tech.*
Received Date:	19 October 2021
Revised Date:	9 December 2021
Accepted Date:	19 December 2021

Please cite this article as: { doi: https://doi.org/

Fatigue Behavior and Modeling of Additively Manufactured IN718: The Effect of Surface Treatments and Surface Measurement Techniques

Seungjong Lee[1,2], Shuai Shao[1,2], Douglas N. Wells[3], Miroslav Zetek[4], Miloslav Kepka[4], Nima Shamsaei[1,2*]

[1] Department of Mechanical Engineering, Auburn University, Auburn, AL 36849, USA

[2] National Center for Additive Manufacturing Excellence (NCAME), Auburn University, Auburn, AL 36849, USA

[3] NASA Marshall Space Flight Center, Huntsville, AL 35812, USA

[4] Regional Technological Institute, University of West Bohemia, Univerzitní 8, 30614 Pilsen 30614, Czech Republic

*Corresponding Author:
Email: shamsaei@auburn.edu
Tel: 334.844.4839

Submitted to:
Journal of Materials Processing Technology

Original Submission: October 2021

Revised Submission: December 2021

Graphical abstract

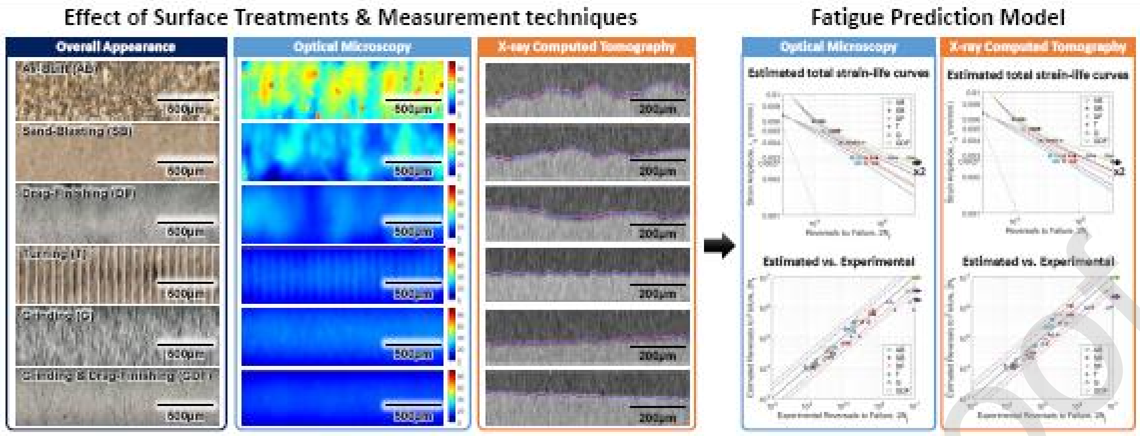

Highlights

- Effect of five surface treatments on surface topography of LB-PBF IN718 was studied
- Surface measurements using optical microscopy and X-ray CT (XCT) were compared
- Surface profiles were constructed from XCT images by curving-fitting edge detection
- The effect of surface roughness was more significant in high cycle fatigue regime
- A modified fatigue notch factor model correlated surface parameters with fatigue life

Abstract

In this study, the effect of various surface treatments, including sand-blasting, drag-finishing, turning, grinding, and grinding + drag-finishing, on surface roughness and fatigue properties of laser beam powder bed fused Inconel 718 was examined. The surface roughness values obtained from two surface measurement techniques, i.e., optical microscopy and X-ray computed tomography, were compared. Both surface measurement techniques consistently indicated that all surface treatments led to improvements in surface roughness, although optical microscopy was influenced by surface glares and overestimated the surface roughness values of drag-finished specimens. Accordingly, all surface treatments also led to improvement in fatigue resistance with sand-blasting and drag-finishing yielding the least while grinding + drag-finishing causing the most. Notably, only the cracks of grinding + drag-finished specimens initiated from crystallographic facets while those in other conditions were surface initiated. Furthermore, by treating the surface valleys as micro notches, an effective fatigue notch factor model using a hybrid surface roughness metric that incorporates several standard surface roughness parameters was shown to correlate the fatigue lives of 94% of specimens with various surface conditions within a scatter band of three.

Abbreviations

AB	As-built
AM	Additive manufacturing/additively manufactured
CM	Conventional manufacturing/conventionally manufactured
DF	Drag-finishing/drag-finished
G	Grinding/ground
GDF	Grinding + drag-finishing/ground + drag-finished
HCF	High cycle fatigue
IN718	Inconel 718
LB-PBF	Laser beam powder bed fusion
LCF	Low cycle fatigue

OM	Optical microscope/optical microscopy
SB	Sand-blasting/sand-blasted
SEM	Scanning electron microscope/scanning electron microscopy
SR	Surface roughness
T	Turning/turned
XCT	X-ray computed tomography

Keywords: Laser beam powder bed fusion (LB-PBF/L-PBF); Post surface treatment; Surface roughness; Fatigue modeling; Fatigue

Nomenclature

b	Fatigue strength exponent
c	Fatigue ductility exponent
R_a/S_a	Arithmetical mean height of the profiled line/area
R_{ku}/S_{ku}	Kurtosis of the profiled line/area
R_{mode}/S_{mode}	Distance between the mean and the mode of the profiled line/area
R_p/S_p	Maximum peak height of the profiled line/area
R_{sk}/S_{sk}	Skewness of the profiled line/area
R_v/S_v	Maximum valley depth of the profiled line/area
ε_a	Strain amplitude
ε_{ea}	Elastic strain amplitude
ε_{pa}	Plastic strain amplitude
ε'_f	Fatigue ductility coefficient
σ_a	Stress amplitude
σ'_f	Fatigue strength coefficient
$2N_f$	Reversals to failure
$\overline{K}_t$	Effective elastic stress concentration factor
$\overline{K}_f$	Effective fatigue notch factor
$\overline{q}$	Notch sensitivity of the material
n	Stress state
γ	Material characteristic length
$\overline{\rho}$	Effective radius of curvature

1. Introduction

Inconel 718 (IN718) is a primarily γ" precipitation hardening alloy and finds use in harsh environments such as gas turbines and oil/gas applications due to its excellent mechanical properties at both room and elevated temperatures and acceptable corrosion resistance (Hosseini and Popovich, 2019). These applications also often require the alloy to be fabricated into complex shapes and associate with high production cost, which is exacerbated with IN718's poor machining characteristics (Rahman et al., 1997). Metal additive manufacturing (AM) provides remarkable advantages in contrast with traditional/subtractive manufacturing methods (Frazier, 2014), the most notable one of which perhaps is its ability to fabricate near-net-shape components with complex geometries. Other benefits brought forth such as light-weighting by topological optimization and fabricating custom-shaped implants on demand have attracted significant interest from both aerospace and biomedical industries.

AM technologies are attractive for alloys with poor machinability since the near-net shaped parts can significantly reduce the need for post process machining (Yin et al., 2020). They are especially promising for IN718, given its good compatibility with additive manufacturing (AM) processes (i.e., good weldability) (Jia and Gu, 2014). Accordingly, the microstructure and mechanical properties of IN718 in various AM forms have been extensively evaluated recently, as reviewed by Kok et al. (2018). For example, the quasi-static mechanical properties of AM IN718 were shown by Wang et al. (2012) to often exceed those of its wrought counterparts after appropriate post process heat treatment. This is the case even with the presence of the as-built (AB) roughness surface.

The fatigue properties of IN718, on the other hand, are very sensitive to the surface finish Gockel et al. (2019). In the machined surface condition, barring the occurrence of exceedingly large volumetric defects (> ~100 μm) (Johnson et al., 2017), the fatigue failures of AM IN718 typically originate from crystallographic slip bands and the fatigue resistance is comparable, if not superior, to that of the wrought forms (Muhammad et al., 2021). However, the AB surface of AM parts comprises stair effects (Hong et al., 2005) from the layer-by-layer fabrication process and partially melted particles and is significantly more detrimental than the volumetric defects. In fact, with the presence of AB surface, fatigue cracks always initiate from the surface micro-notches (Balachandramurthi et al., 2018). The fatigue lives of specimens in the AB surface condition were often reported to be significantly lower than the specimens with machined surfaces suggesting a need for surface machining for parts in fatigue critical applications. Interestingly, due to the unique spatial distribution of AM defects in an AM part, machining does not always improve fatigue performance. The low energy density contour scan on each layer and overheating during the return of tracks can lead to a significantly higher density of defects such as lack of fusions (Tang et al., 2017) and keyholes (King et al., 2014) near the surface. Therefore, shallow surface machining, which is often desirable for IN718 due to its poor machinability, can expose these defects as detrimental surface notches (Zhao et al., 2021).

Aside from constraints imposed by IN718's machinability, conventional surface machining techniques, such as milling, turning, and grinding, are sometimes not feasible due to the complex geometries of the parts (Maleki et al., 2020) or not desired since rough surfaces are sometimes required by skeletal implants for better biocompatibility (Singh and Ramakrishna, 2017). In such cases, non-conventional surface treatment alternatives may be needed. For instance, the working principles of drag-finishing relies on coarse granular materials which is not subjected to the conventional tool access constraints (Barletta et al., 2014). Also, sand-blasting can induce compressive residual stresses helping tolerate a considerable SR (Krawczyk et al., 2016).At present, the effect of various surface treatments on fatigue behavior has only been investigated for some alloys, such as Ti-6Al-4V (Kahlin et al., 2020). A thorough investigation of the effect of different types of surface treatment on both SR and fatigue properties of AM IN718 is still much needed.

Among different SR measuring techniques available, such as optical microscopy (OM) based, stylus based, and X-ray computed tomography (XCT) based methods, the non-tactile ones are often preferred over the stylus based methods, as the latter relies on sharp stylus tips to access the fine details on the surfaces which may not be feasible. In addition, different SR measurement methods do not necessarily produce the same SR values for the same area of interest. This is especially the case for AB surfaces of AM parts which are typically decorated with surface-connected pores and over-hang structures whose true features are not always in the line of sight (Hamidi Nasab et al., 2019). Moreover, XCT scans are constrained by the resolution (voxel size)-scan volume tradeoff and scanning an area of meaningful size often requires the voxel to be bigger, sacrificing the accuracy of SR measurement. Although OM- and XCT- based SR measurements were shown to yield comparable results for AB surfaces (Gockel et al., 2019), the efficacy of XCT-based methods on resolving features whose dimension approaching or smaller than the voxel size has not been evaluated.

This study investigates the effect of various post process surface treatment techniques on the SR of AM IN718 specimens and, in turn, their influence on fatigue performance. The specimens were fabricated using laser beam powder bed fusion (LB-PBF) with default process parameters from the machine manufacturer. After fabrication, all specimens went through heat treatments including stress relief, solution treatment, and two-step aging. Five different post surface treatments (including sand-blasting, drag-finishing, turning, grinding, and grinding +

drag-finishing) were performed on specimens and the surface of each condition was characterized. Surface topographies of each condition were measured by OM and XCT. In addition, strain-controlled followed by force-controlled fatigue tests were conducted to investigate the axial fatigue behaviors of specimens with various surface conditions. Finally, the strain-life behavior of the specimens was modeled with the reference of the mirror-polished specimens using a modified fatigue notch factor approach (Lee et al., 2021), which was developed in the authors' previous study to incorporate a hybrid SR parameter.

2. Materials and methods

2.1. Fabrication

The design of the specimens, shown in Fig. 1, for strain-controlled fatigue testing follows ASTM E606 with the exception of the gage diameter (ASTM E606, 2021). The specimens were fabricated using an EOS M290 LB-PBF machine in the argon atmosphere. The default process parameters provided by the manufacturer of the EOS M290 were used: laser power of 285W, laser scanning speed of 960 mm/s, hatching space of 110 μm, and layer thickness of 40 μm. The specimens were stress relieved (1065°C ± 14^{0} C for 1.5 hours followed by furnace cooling) before they were removed from the substrate. Further heat treatments included a solution treatment and a two-step aging in accordance with SAE AMS 5564 (holding at 1065°C ± 14^{0} C for 1 hour, argon quenching, precipitation aging at 760^{0} C ± 8^{0} C for 10 hours ± 0.5 hours, furnace cooling to 650^{0} C ± 8^{0} C and holding for a total precipitation time of 20 hours) (AMS 5564, 2013).

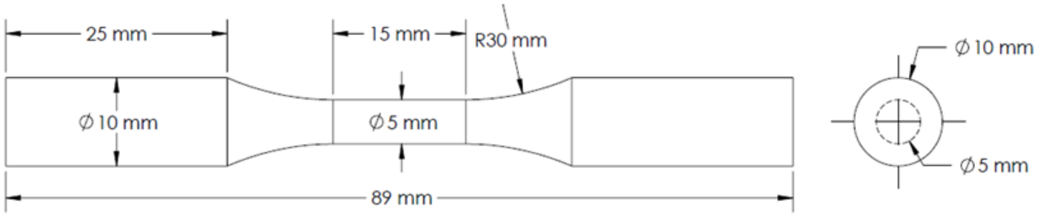

Fig. 1 Specimen geometry and dimensions for strain-controlled fatigue tests.

2.2. Post process surface treatments

Various post surface treatments including drag-finishing (DF), grinding (G), grinding + drag-finishing (GDF), sand-blasting (SB), and turning (T) with positive cutting inserts geometry were conducted on five batches of specimens, while one batch was kept in AB surface condition. The process parameters used in this study for post surface treatment were empirically optimized based on the prior post surface treatment experience on such alloys at Regional Technological Institute of University of West Bohemia. The procedure and process parameters of each post surface treatment are provided briefly in the following paragraphs.

DF rotates specimens within the working media mass which results in honing and polishing effects. In this study, OTEC DF3 unit with HSC 300 media consisting of walnut shell granules were utilized for DF. In the OTEC DF3 unit the specimens' grips were held by the self-rotating grip holders (called disk). Mounted on a rotor, the disks also revolved around the rotor's axis. The empirically optimized process parameters used in this study were: disk rotation speed of 45 rpm, rotor rotation speed of 45 rpm, depth in media of 400 mm, and total processing time of 240 mins.

SB was conducted using the Graf system using the corundum particles with a mesh size of 320 and the fluid pressure of 280 kPa. The specimens were placed into the holder that was rotated by the base planetary gears around the main axis. T was conducted with the following process parameters: cutting speed of 25 rpm, feed rate of 0.1 mm/s, and depth of 0.25 mm. For the G process, the ANCA MX 7 5 axes grinding machine with the Cafro B46 S 200 GAL grinding wheel was used. The final grinding process parameters were: grinding speed of 6366 rpm, grinding feed rate of 100 mm/min, workpiece rotation speed of 1206 rpm, and cutting depth of 0.01 mm.

Among these post process surface treatments, DF and SB can be categorized as non-subtractive methods that do not substantially remove material which is in contrast to the subtractive methods such as G and T. While the diameter of the gage section of specimens in the AB condition and after non-subtractive methods was ~5 mm, the diameter after subtractive methods was reduced to ~4 mm.

2.3. Surface measurements

The specimen surfaces for each surface condition were investigated using an OM (Keyence VHX-6000X) and an XCT system (ZEISS Xradia 620 Versa). According to Lee et al. (2021), the difference between SR measured using the OM with 500X and 1000X magnifications is negligible. Therefore, the gage section of specimens was measured at 500X magnification and each pixel size was 0.43 μm. The captured 3D images were converted via image stacking techniques into height data stored in CSV files. Further analysis to obtain surface topographies and SR values was processed using MATLAB. In addition, surface XCT measurements were conducted with voxel sizes of 1.98 μm and 0.58 μm. The raw XCT files were reconstructed using Zeiss software and saved as TIFF images representing radial slices through the specimen which can be "resliced" to reveal the longitudinal sections. Figure 2 illustrates how a 2D surface topography of a longitudinal slice of the specimen was converted from a 3D XCT. Two different image post processing techniques were attempted: a manual approach that required binary images and an automated approach directly using the gray scale images.

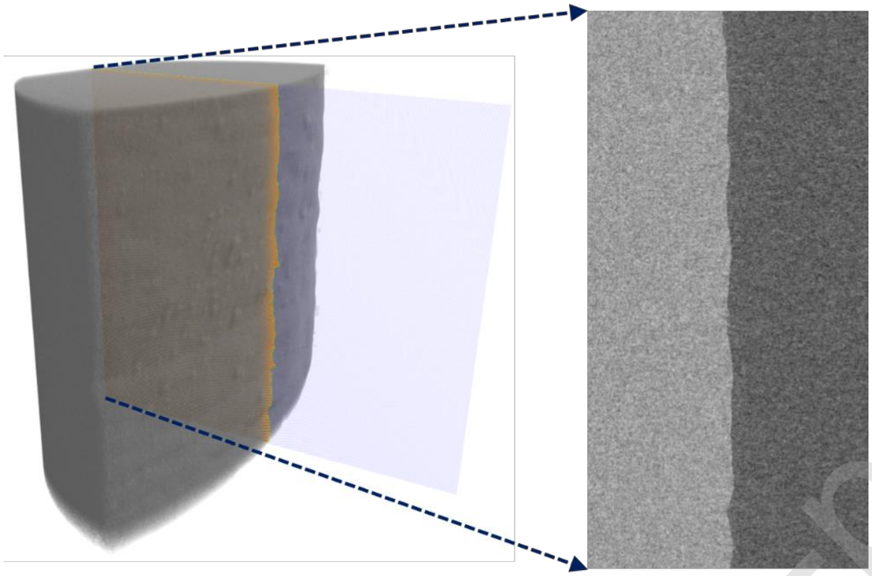

Fig. 2 Schematic showing how a 2D surface topography of the longitudinal slice of the specimen was converted from a 3D surface topography.

The manual approach (procedure illustrated in a red box in Fig. 3) utilized ImageJ as a mid-processor to generate the binary image of the edges. The as-reconstructed, 16-bit TIFF images were processed using a 3D gradient function to detect edges. This image was further processed through a thresholding algorithm to create a binary image; however, the obtained binary images contained inevitable noise that could not be automatically filtered. This noise was removed manually. The final binary images, free of noise, were analyzed by MATLAB to obtain the surface topography and roughness.

On the other hand, the automated approach (procedure illustrated in a blue box in Fig. 3) was conducted directly from gray scale images by fitting the intensity values along traces on the specimens' radial direction with logistic curves per Eq. (1) following the well-established curve fitting based edge detection algorithms (Xu, 2009). The raw TIFF images reconstructed from x-ray projections were directly imported, read, and analyzed using MATLAB, which produced the final line profiles. The imported raw TIFF image had X-ray absorption data for each pixel, i.e., higher values representing high X-ray absorption and vice versa. An edge was detected by finding the maximum of the first derivative of the fitted logistic function as shown in Fig. 3. The logistic function is expressed in Eq. (1):

$$y = A_2 + \frac{(A_1 - A_2)}{1 + (\frac{x}{x_0})^p} \tag{1}$$

where A_1 is an initial value, A_2 is a final value, x_0 is a center, and p is power. In principle, the accuracy of edge location detected by this approach can be sub-voxel. This procedure is repeated for radial lines at different z positions to obtain a line profile of the surface texture along the axis of the specimen.

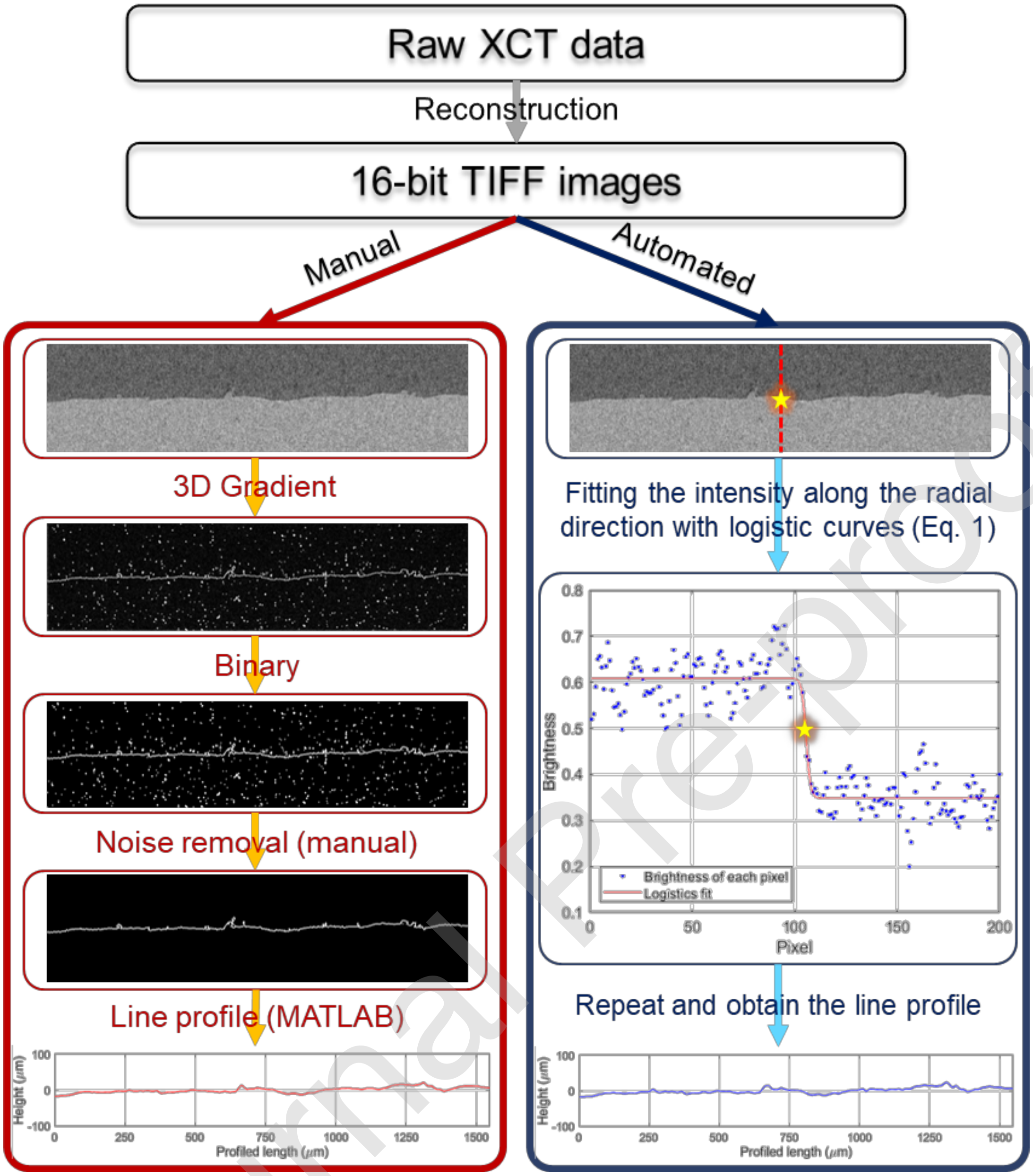

Fig. 3 Flow charts of both manual and automated approaches to explain how line profiles are extracted from raw XCT images.

2.4. Fatigue tests and fractography

Fully reversed strain-controlled fatigue tests were conducted following ASTM E606 using a servo-hydraulic fatigue machine. Acrylic paint was applied to the areas where the extensometer was attached to the gage of the specimen to avoid any chance of slip. Purely elastic deformations were observed in the test with ε_a = 0.004 mm/mm and below. Therefore, the tests with ε_a = 0.004 mm/mm and below were started in strain-control mode and converted to force-control mode after ~10,000 cycles. If the running cycles reached 10 million, the test was suspended and considered as runouts. The fractured surfaces after fatigue tests were examined using a scanning electron microscope (SEM).

3. Experimental results

3.1. Surface measurements

3.1.1. Optical microscope

The surface topography of each surface condition and corresponding line profiles are distinctive as shown by the surface height maps from OM in Fig. 4. For a better understanding of each surface condition, overall specimens' appearance from OM is provided in Fig. 5. The AB surface has partially melted powder particles attached which are depicted as peaks in Fig. 4(a). As shown in Figs. 4(b) and 4(c), SB and DF treatments are effective to remove remaining particles but cannot fully remove underlying surface waviness resulting from the layer-by-layer AM process. The surface topographies after subtractive surface treatments (T, G, and GDF) are significantly smoother compared to non-subtractive methods (SB and DF). The turned surface (Fig. 4(d)) shows clear and regularly spaced machining marks. Although machining marks are also visible in the ground surface (Fig. 4(e)), their spacing is much smaller and irregular. As shown in Fig. 4(f), drag finishing can completely remove the fine machining marks left by grinding, leaving the smoothest surface finish among all seven surface treatment techniques. The GDF surface will be assumed as notch free and used as the reference surface condition in this study for the fatigue notch factored based analysis.

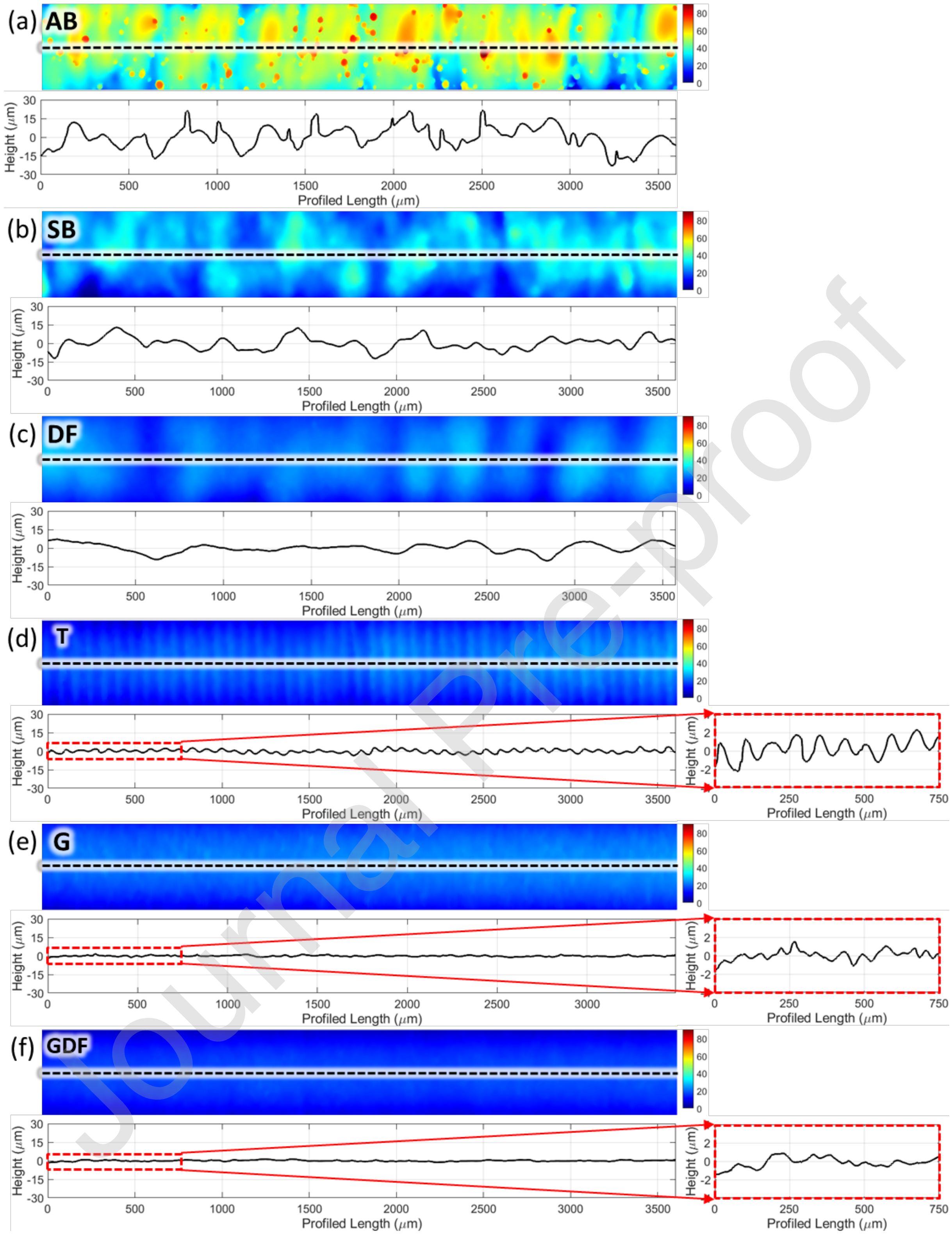

Fig. 4 Surface topography color maps and corresponded line profiles of (a) AB, (b) SB, (c) DF, (d) T, (e) G, and (f) GDF conditions captured by the OM.

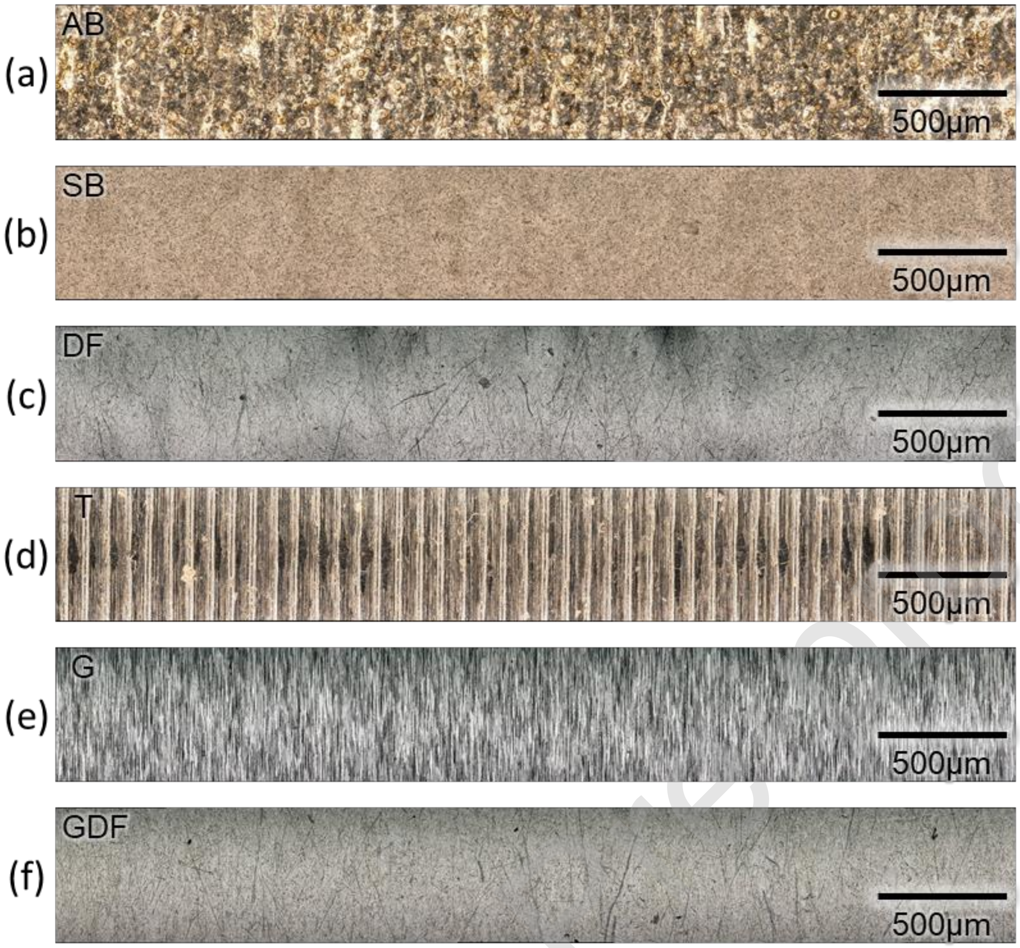

Fig. 5 Overall appearances of (a) AB, (b) SB, (c) DF, (d) T, (e) G, and (f) GDF conditions captured by the OM.

The line profiles for subtractive treatment conditions; i.e., T, G, and GDF, are significantly flatter than those for non-subtractive treatments conditions; i.e., SB and DF. The magnified view of small portions of the line profiles of T, G, and GDF conditions are provided in Fig. 4 to offer better comparisons. Among the surfaces after subtractive post surface treatments, T condition again showed the roughest surface. The difference between G and GDF is also evident based on the profiles obtained from optical 3D surfaces with the GDF exhibiting lower amplitude and smaller curvatures in the groves/peaks. Based on 3 line profiles with a 107 μm interval within a scanned image, standard SR parameters according to the ISO 4287:1997 (ISO

4287, 1997) and hybrid SR parameters proposed by Lee et al. (2021) of all surface conditions are calculated and listed in Table 1. It is confirmed that the surface after GDF has the lowest SR values among all conditions.

Table 1 Standard and hybrid SR parameters generated by height data measured by OM.

Surface Condition	**R_a (μm)**	**R_p (μm)**	**R_v (μm)**	**R_{sk}**	**R_{ku}**	**R_{mode} (μm)**	**R_v+R_{mode} (μm)**	**R_v+R_{mode}×R_{sk}×R_{ku} (μm)**
AB	4.35	13.73	12.42	0.39	2.82	-2.08	10.34	14.95
SB	3.14	9.68	9.91	0.05	2.84	-0.65	9.26	9.76
DF	2.71	7.68	7.85	0.00	2.59	-0.94	6.90	8.61
T	1.08	3.55	3.45	0.02	2.64	-0.25	3.21	3.47
G	0.37	1.31	1.29	0.07	3.13	0.02	1.31	1.28
GDF	0.31	1.11	1.10	-0.14	2.81	0.02	1.13	1.15

3.1.2. Computed tomography

Two different approaches; i.e., manual approach with the binary images and automated approach with gray scale images, were utilized to analyze the same XCT scans. Figure 6 presents line profiles obtained from both approaches overlaying with the gray scale absorption images. Consistent with the observations from OM based SR measurements, the surface after subtractive treatments (i.e., T, G, and GDF conditions) again shows smoother line profiles from the scan with a voxel size of 1.98 μm. It is evident from Figs. 6(d), 6(e), and 6(f) that magnitude of some of the fluctuations in these conditions are approaching the voxel size of 1.98 μm; therefore, making them challenging to resolve in these scans. As such, the T, G, and GDF surfaces were scanned again with a voxel size of 0.58 μm and the obtained line profiles are shown on the right side of Fig. 6 as Figs. 6(d'), 6(e'), and 6(f'). The standard and hybrid SR are calculated using the line profiles from the manual and automated approaches and listed in Tables 2 and 3, respectively. The results confirm that differences between SR measured by the manual and automated approaches are negligible.

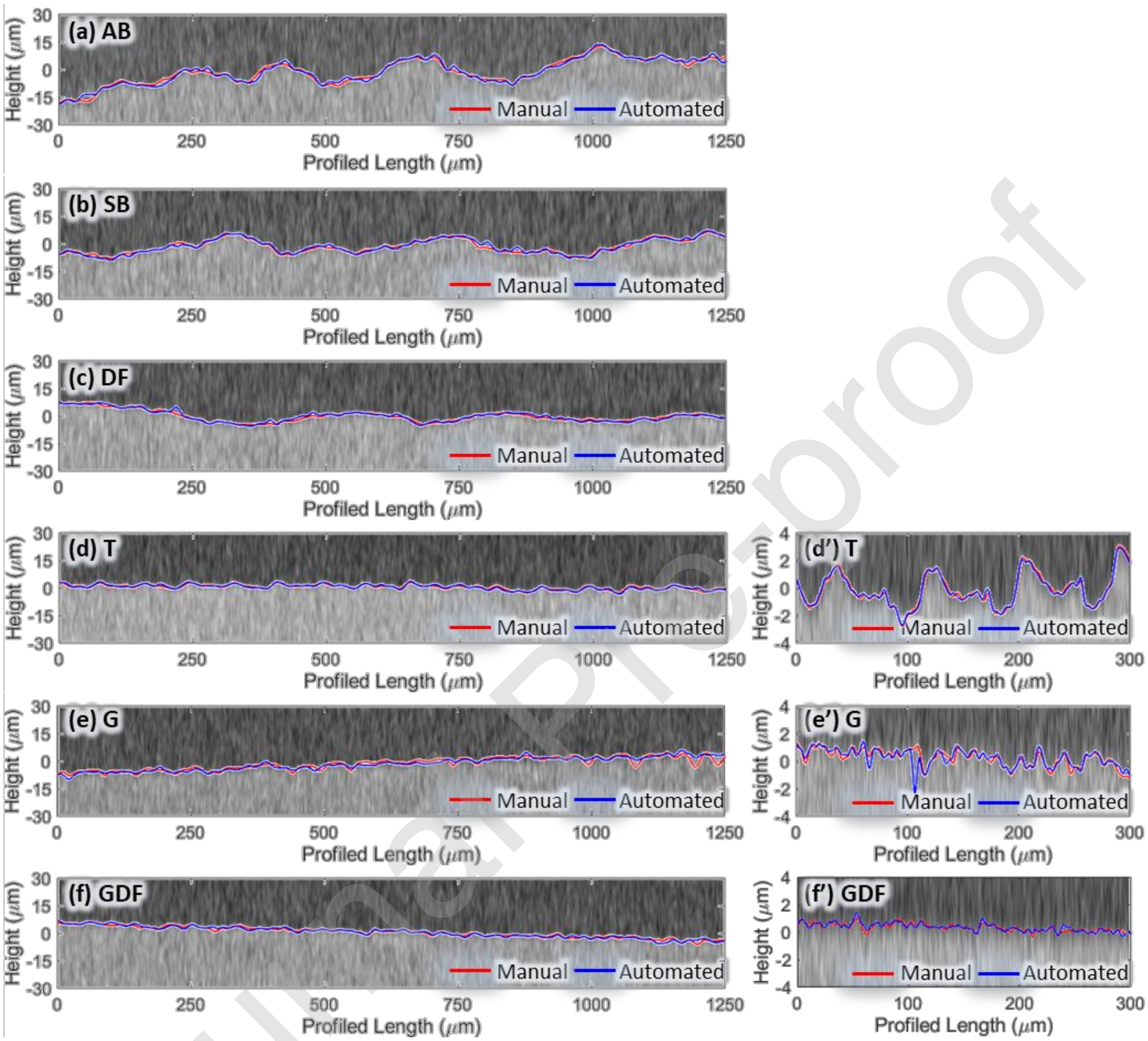

Fig. 6 Raw TIFF images scanned by XCT with overlapped line profiles using the manual (red lines) and the automated (blue lines) approaches for every surface condition: (a) AB, (b) SB, (c) DF, (d) T, (e) G, and (f) GDF conditions. Results from the higher-resolution scans (at a smaller voxel size of 0.58 μm) for subtractively treated surfaces: (d') T, (e') G, and (f') GDF conditions.

Table 2 SR parameters calculated using line profiles measured by the XCT with the manual approach.

Surface	R_a	R_p	R_v	R_{sk}	R_{ku}	R_{mode}	R_v+R_{mode}	$R_v+R_{mode}\times R_{sk}\times R_{ku}$

Condition	(µm)	(µm)	(µm)			(µm)	(µm)	(µm)
AB	3.96	11.59	13.16	-0.20	2.96	2.31	15.47	14.39
SB	3.20	8.29	9.57	-0.18	2.60	1.53	11.10	9.75
DF	2.27	6.38	5.84	0.13	2.62	0.51	6.35	5.77
T	0.77	2.34	2.40	0.05	2.64	-0.19	2.21	2.49
G	0.92	2.36	1.69	-0.53	3.27	0.95	2.64	3.56
GDF	0.52	1.81	1.49	-0.26	3.17	0.17	1.67	1.66

Table 3 SR parameters calculated using line profiles measured by the XCT with the automated approach.

Surface Condition	R_a (µm)	R_p (µm)	R_v (µm)	R_{sk}	R_{ku}	R_{mode} (µm)	R_v+R_{mode} (µm)	R_v+R_{mode}×R_{sk}×R_{ku} (µm)
AB	4.04	12.22	13.08	-0.11	2.91	0.23	13.31	13.07
SB	3.21	8.42	9.26	-0.19	2.55	-0.30	8.96	10.20
DF	2.23	6.51	5.96	0.13	2.59	0.41	6.37	5.93
T	0.86	2.93	2.67	0.08	2.67	-0.11	2.56	2.75
G	0.60	2.13	2.11	-0.11	3.03	0.12	2.23	2.12
GDF	0.55	1.83	1.89	-0.15	2.76	0.08	1.97	1.98

While the obtained line surface profiles and calculated SR parameters from manual and automated approaches are similar, the automated method is significantly more streamlined, and therefore, is preferred. Since the automated approach does not require any additional efforts such as gradient and binary processes, the finalized algorithm (e.g., MATLAB code) can be utilized directly from raw TIFF image reconstructed for every XCT scan. The automated approach is free of any manual operations (e.g., noise removal) and is, therefore, more robust and not subject to human errors.

3.2. Fatigue performance

The strain-controlled followed by force-controlled fatigue testing results are listed in Table 4. The stresses are calculated by dividing the applied loads by the areas of circles inscribed within the perimeters on the radial cross sections of specimen gages (Pegues et al., 2018). The diameter of these circles is estimated by measured value using caliper followed by subtracting twice of maximum peak height to maximum valley depth of the profiled line. Mean stresses are less than 10% of stress amplitudes, so no effect of mean stresses is expected. Based on Table 4, the strain-life plot is generated as shown in Fig. 7. As seen in Fig. 7, the fatigue lives of specimens with different surface conditions significantly overlap at $\varepsilon_a = 0.006$ mm/mm. The data of T specimens at $\varepsilon_a = 0.006$ mm/mm, as an example, has a variation of a factor of two with one data point showing shorter fatigue live than the AB specimens. A similar trend is observed in the data at $\varepsilon_a = 0.005$ mm/mm except for one outlying AB data point. These observations align with the assumption that the effect of SR on fatigue behavior of LB-PBF IN718 is relatively small in the LCF regime, where the fatigue behavior is known to be dominated by crack growth in general (Lee et al., 2020).

The difference in fatigue lives among different surface conditions increases as the applied strain amplitude decreases since the governing mechanisms transition from crack growth to crack initiation. For example, at the $\varepsilon_a = 0.004$ mm/mm, where there is a lack of plastic strain, fatigue lives between non-subtractive and subtractive methods become relatively separated. Notably, the fatigue lives under the applied strain amplitudes less than 0.003 mm/mm appear to segregate into two groups; i.e., the surfaces treated with non-subtractive processes (SB and DF) and those subjected to subtractive processes (T, G, and GDF), while AB specimens consistently exhibit the shortest fatigue lives. All surface-treated specimens with subtractive material removal reach runout (i.e., 10^7 reversals) at $\varepsilon_a = 0.0027$ mm/mm. In addition, more than 2 orders of magnitude difference in fatigue lives can be noticed at $\varepsilon_a = 0.0027$ mm/mm.

Table 4 Strain-controlled followed by force-controlled fatigue testing results.

Surface condition	**Area (mm^2)**	**Frequency (Hz)**	**Strain Amplitude, ε_a (mm/mm)**	**Stress Amplitude, σ_a (MPa)**	**Mean Stress, σ_m (MPa)**	**Reversals to Failure, $2N_f$**
AB	18.27	0.83	0.0060	1019	-1	9,476
	18.27	0.83	0.0060	1003	-56	11,852
	18.07	1.00	0.0050	934	14	18,716
	18.47	1.00	0.0050	893	13	29,774
	18.40	1.25	0.0040	747	25	58,866
	18.32	1.25	0.0040	750	-50	69,412
	18.55	1.67	0.0030	560	-6	123,126
	18.22	1.67	0.0030	574	1	128,464
	18.60	1.85	0.0027	502	-8	163,544
	18.53	1.67	0.0030	536	33	190,840
	18.40	1.85	0.0027	503	-3	202,756
	18.22	1.85	0.0027	513	-18	206,020
SB	18.10	0.83	0.0060	1020	-51	14,036
	18.12	0.83	0.0060	1004	-36	16,738
	18.10	1.00	0.0050	922	7	41,790
	18.02	1.00	0.0050	928	-32	52,826
	18.10	1.25	0.0040	713	10	103,610
	18.15	1.25	0.0040	758	4	141,562
	18.17	1.85	0.0027	506	-2	325,626
	18.00	1.67	0.0030	554	-21	328,458
	18.27	1.67	0.0030	550	-2	485,124
	18.10	1.85	0.0027	507	-5	558,182
	18.20	1.67	0.0030	561	-16	689,322
	18.12	1.85	0.0027	511	-4	731,240
DF	17.80	0.83	0.0060	1008	-17	13,316
	17.87	0.83	0.0060	1007	-12	15,438
	17.65	1.00	0.0050	925	-26	33,998
	18.10	1.00	0.0050	914	-20	37,966
	17.90	1.25	0.0040	756	-33	114,960
	17.97	1.25	0.0040	721	-32	132,688
	17.72	1.67	0.0030	585	-44	248,562
	17.80	1.67	0.0030	562	-8	344,324
	17.87	1.67	0.0030	554	-14	513,708
	17.87	1.85	0.0027	509	-13	525,764
	18.05	1.85	0.0027	502	-17	629,106
	18.22	1.85	0.0027	509	0	743,828
T	11.76	0.83	0.0060	1073	-55	8,932

	11.76	0.83	0.0060	1033	-26	15,298
	11.84	1.00	0.0050	983	-34	49,932
	11.97	1.00	0.0050	949	-20	59,898
	11.66	1.25	0.0040	833	-3	159,598
	11.52	1.25	0.0040	838	-3	279,600
	11.74	1.67	0.0030	610	10	689,658
	11.84	1.67	0.0030	607	-8	2,819,292
	11.95	1.67	0.0030	586	-3	9,791,014
	11.97	1.85	0.0027	530	-18	>10,000,000
	11.88	1.85	0.0027	532	-9	>10,000,000
G	11.32	0.83	0.0060	1032	-37	18,188
	12.01	0.83	0.0060	1019	-36	20,050
	11.16	1.00	0.0050	985	17	38,928
	12.27	1.00	0.0050	916	-49	53,396
	12.01	1.25	0.0040	783	-4	200,042
	11.93	1.25	0.0040	783	6	203,256
	12.07	1.67	0.0030	594	-5	1,746,332
	12.09	1.67	0.0030	584	-37	2,221,876
	12.19	1.67	0.0030	579	-25	7,517,084
	11.99	1.85	0.0027	531	-9	>10,000,000
	11.99	1.85	0.0027	523	-7	>10,000,000
GDF	11.95	0.83	0.0060	1024	-46	15,044
	11.84	0.83	0.0060	1037	-34	17,292
	12.01	1.00	0.0050	956	-11	33,416
	11.94	1.00	0.0050	954	-13	45,256
	11.88	1.25	0.0040	784	-14	177,774
	11.88	1.25	0.0040	802	8	197,002
	12.27	1.67	0.0030	576	-15	6,202,684
	11.91	1.67	0.0030	593	7	6,286,240
	12.00	1.67	0.0030	596	11	7,060,592
	12.11	1.85	0.0027	526	0	>10,000,000
	11.86	1.85	0.0027	540	3	>10,000,000

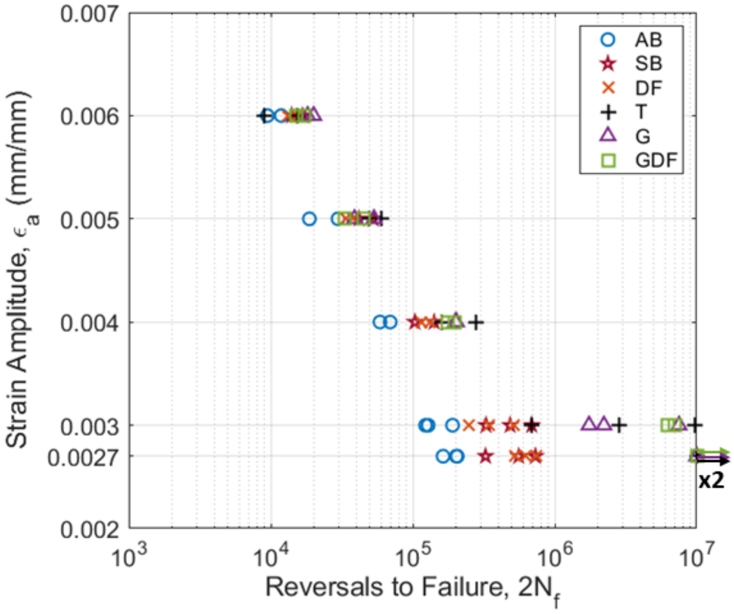

Fig. 7 Strain-life fatigue tests results.

Figures 8(a) and (b) show the hysteresis loops of AB specimens which have the roughest surface and GDF specimens which have the smoothest surface, respectively. As expected, the surface conditions do not appreciably affect the hysteresis response. The obtained plastic strain amplitudes (ε_{pa}) are ~0.0007 mm/mm and ~0.0002 mm/mm at ε_a = 0.006 mm/mm and ε_a = 0.005 mm/mm, respectively, for both AB and GDF surface conditions. The ε_{pa} vanishes for ε_a below 0.004 mm/mm. The quasi-static tensile curve and cyclic stress-strain data, based on the obtained plastic strain amplitudes from hysteresis loops, are shown in Fig. 8(c). Both cyclic stress-strain data of AB (red dotted line) and GDF (blue dotted line) specimens are below the quasi-static curve (black solid line) which means that cyclic softening occurred regardless of the surface condition. This is expected since the cyclic stress-strain behavior is more affected by material properties rather than surface conditions (Stephens et al., 2000).

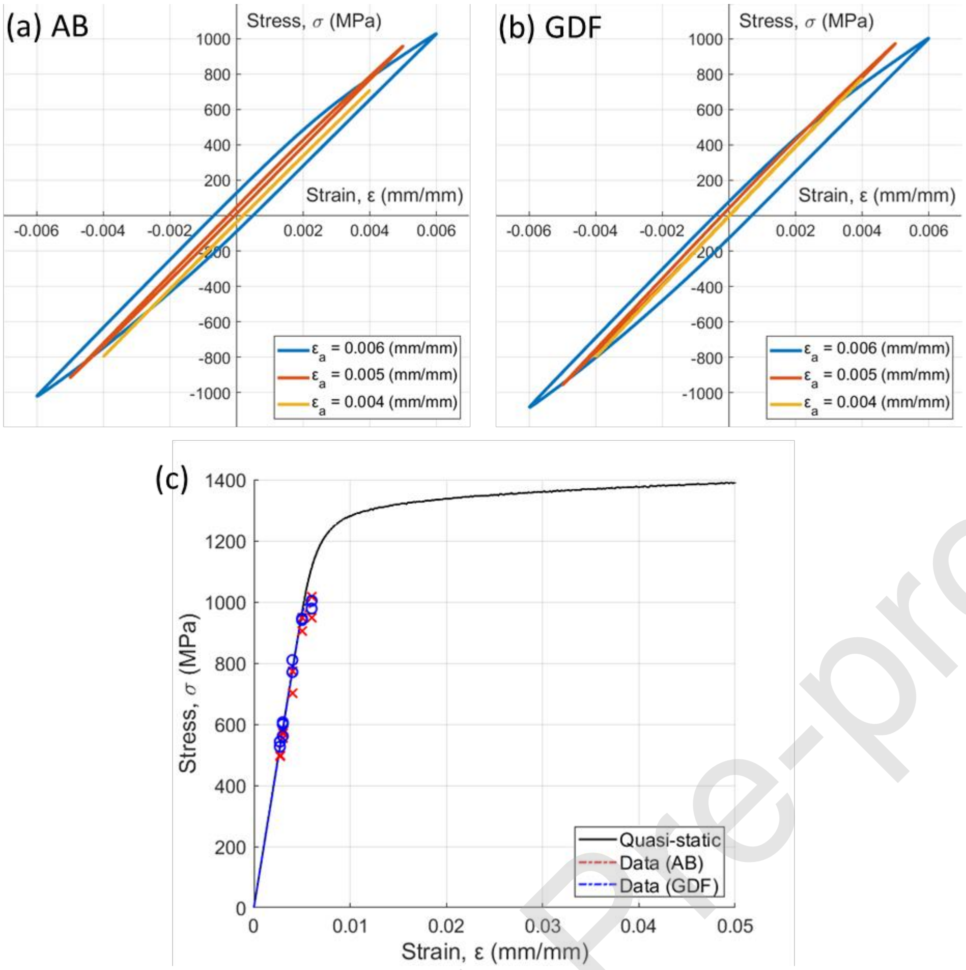

Fig. 8 Cyclic stress-strain hysteresis loops of specimens in (a) AB and (b) GDF surface conditions. (c) Quasi-static tensile curve and cyclic stress-strain data of specimens in AB and GDF surface conditions.

3.3. Fractography

The representative SEM images of the final fractured surfaces of each condition are shown in Fig. 9, with magnified views of crack initiation sites. As shown in Figs. 9(a), (b), and (c), the main cracks of AB as well as SB and DF treated specimens initiated from the specimen surface. Even though the AB surface was fully removed by the subtractive surface treatments, the T and G specimens (Figs. 9(d) and (e)) still had crack initiations from the surface. It should be noted that after machining processes (e.g., T and G), there are still some surface grooves on the surface that are perpendicular to the loading direction, producing stress concentrations that may result in early crack initiations. In contrast, most GDF specimens with much smoother surface conditions had crack initiations from the persistent slip bands, leaving crystallographic facets at the initiation sites on the fracture surface, as shown in Fig. 9(f). Only two GDF specimens had crack initiations from volumetric defects (one was from a keyhole, the other one was from a lack of fusion).

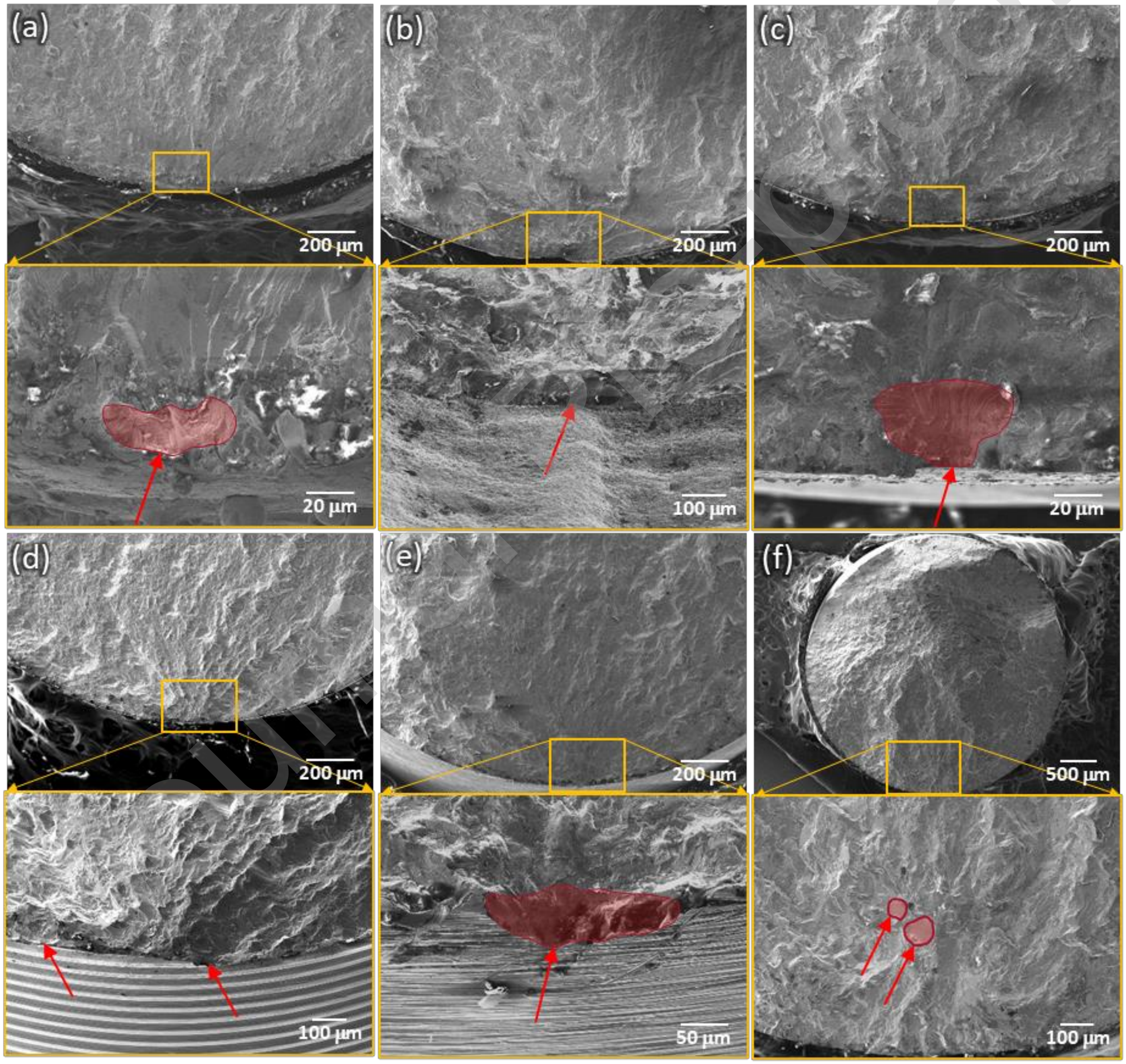

Fig. 9 Fracture surfaces of specimens in each surface condition: (a) AB, (b) SB, (c) DF, (d) T, (e) G, and (f) GDF

In addition to the fractography, a longitudinal cross-section of an AB specimen after fatigue test was polished and examined using SEM as presented in Fig. 10(a), showing a secondary crack initiation, not the dominant crack causing fracture, from the surface. However, the crack initiation site is hidden by an over-hanging structure consisting of a partially melted powder particle in this case. Figure 10(b) displays the feasibility of XCT which can observe the same crack initiated from a hidden valley. As a result, valleys of this nature cannot be detected by stylus based or optical surface profilometry, which suggests that XCT based SR measurement, despite its added costs, are more effective in such scenarios.

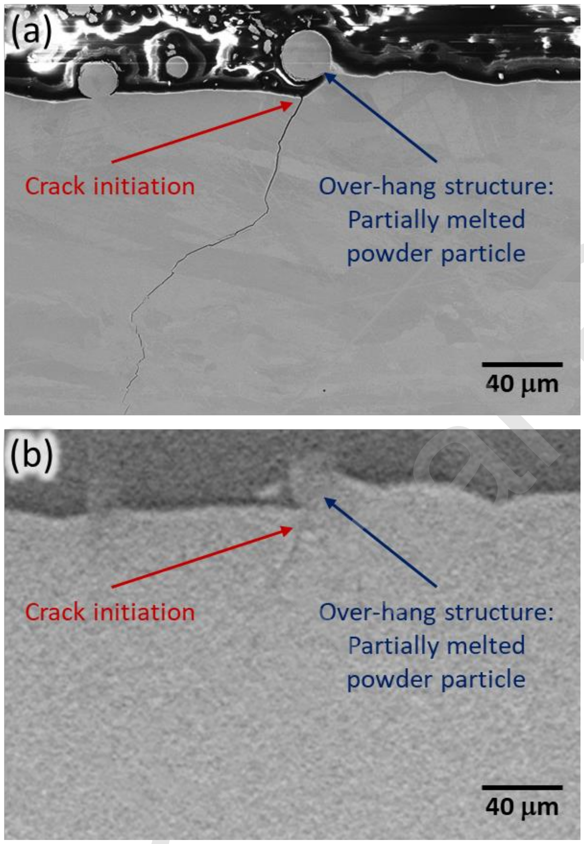

Fig. 10 The polished longitudinal cross-section of an AB specimen after fatigue test showing a secondary crack: captured by (a) SEM and (b) XCT.

4. Discussion

4.1. Comparing surface measurement techniques

The SR parameters measured by OM and XCT showed similar trends that AB has the highest SR values (e.g., R_a and R_v) followed respectively by SB, DF, T, G, and GDF conditions. Figure 11 visualizes the maximum valley depth of line profiles (R_v) from three different techniques (optical method and XCT manual/automated approaches) for each surface condition. While the R_v values obtained from OM and XCT based techniques are relatively consistent (i.e., within a variation of about 7%) with each other for AB and SB treated surface conditions, they are quite different (i.e., more than 29%) for DF, T, G, and GDF treated surfaces. It should be noted that the measuring principle of OM used in this study is based on the physics of the interaction between the light beam and the surface (Leach et al., 2015). As such, the shiny surface left by surface treatment processes, such as DF, T, G, and GDF conditions, can cause more glare compared to AB and SB conditions, which may skew the roughness measurement towards higher values.

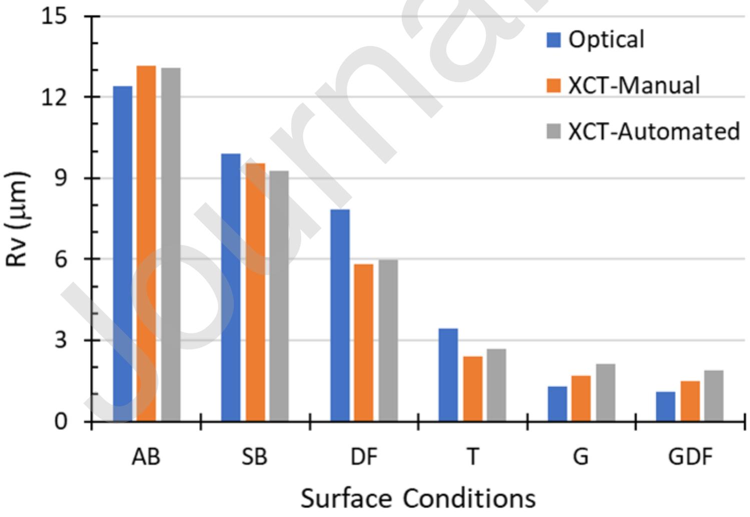

Fig. 11 R_v of each surface condition measured by three different techniques.

To validate this hypothesis, a DF specimen, as a representative, was cut and polished along the longitudinal plane and the line profile was measured using OM. Figure 12 shows the images of the polished longitudinal cross-section of the DF specimen measured by OM and overlaid with a line profile. The measured R_v of DF based on cross-section was 4.45 μm, which is almost half of R_v values from the OM measurement and closer to the measurement from XCT based approaches. Even though the locations where the surface profiles were obtained do not necessarily coincide with those of profiles shown in Figs. 4 and 6, the observations here nevertheless confirm that the optical method can sometimes be influenced by surface glare resulting in misestimated roughness values. The uncertainty of the measurement using OM is more significant for T, G, and GDF surface conditions. This is in agreement with Syam et al. (2019), which discussed the challenges of OM that need to be overcome such as measurement with high spatial bandwidth specifically for materials with specular surfaces. In this regard, Stavroulakis and Leach, (2016) suggested that OM be used to measure AB AM parts and other techniques such as laser triangulation be used for AM parts after surface treatments.

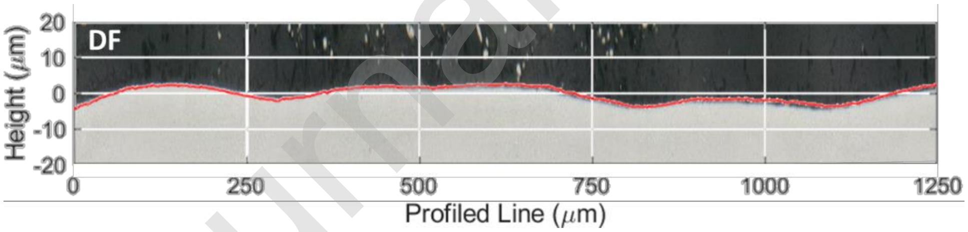

Fig. 12 Polished longitudinal cross-sections overlaid with a line profile obtained using OM for the DF surface condition.

Despite the limitations of the OM associated with their sensitivity to imaging conditions, it is still the most commonly and commercially used technique for SR characterization not only because of its substantially lower cost, but also because of its superior efficiency. For instance, each scan in this study took only a few minutes for OM but a few hours for XCT. The difference in efficiency becomes more notable should there be a need for more scans with different magnification. In addition, at a given resolution, the area that can be scanned by OM is typically far larger than XCT. As an example, the OM used in this study (Keyence VHX-6000X) can scan 7 by 7 mm area with a pixel size of 0.43 μm and 500X magnification, on the other hand, the XCT (ZEISS Xradia 620 Versa) can only scan 0.4 by 0.4 mm area with a pixel size of 0.58 μm. However, if capturing surface-connected pores and valleys hidden by over-hanging particles/structures is required XCT is still recommended.

4.2. Effects of surface treatments on fatigue behavior

The post surface treatments applied in this study can be categorized as non-subtractive methods (SB and DF) and subtractive methods (T, G, and GDF). While the SR values of specimens after SB or DF are not reduced as much as the surface after subtractive methods, they are substantially lower than that of the AB surface condition. The AB surface consists of partially melted powder particles and step-like features due to AM's unique layer-by-layer process (Townsend et al., 2016). The partially melted powder particles appear as peaks on the surface profiles and influence certain SR parameters significantly, including the maximum peak height of the profiled line/area (R_p/S_p) and the arithmetical mean height of the profiled line/area (R_a/S_a).

Tyagi et al. (2019), showed that the reduction of S_p values for both electropolished and chemically-polished surfaces is more significant compared to other SR such as S_a and S_v. It is therefore expected that even if a surface treatment process could only remove the partially melted powder particles attached to the surface, certain SR parameters, such as R_p, may be significantly improved. Indeed, Table 1 shows that R_p is the most significantly reduced value among all SR parameters considered after SB and DF post surface treatments, which suggests that the improvement of surface by non-subtractive methods is mainly driven by removing protruding materials such as partially melted powder particles.

For the same reason, even though some SR metrics can be improved by non-subtractive post surface treatments, the improvement of fatigue strength may not be as significant. Zhang and Fatemi (2019) indicated that R_v/S_v parameter is more indicative of a specimen's fatigue behavior compared to other SR parameters. Indeed, Chan (2015) correlated R_v with the fatigue life of AM Ti-6Al-4V. According to the surface topographies shown in Figs. 4 and 6, the surfaces after SB and DF processes still have wavy features which can act as blunt notches. In comparison, subtractive post surface treatments not only reduced SR parameters sensitive to the presence of peaks such as R_p, but also ones related to the valleys such as R_v and R_a. As seen in Figs. 4 and 6, the approximately ~500 μm of machining depth of subtractive methods is far beyond the maximum height of the AB surface (26 μm from OM and 25 μm from XCT) and have completely removed the topography of the AB surface. As a result, the fatigue resistance of specimens after subtractive surface treatments is substantially improved in the HCF regime due to the more substantial improvement of surface condition including the removal of near-surface AM defects.

Although each of the subtractive methods in this study fully remove the AB surface, they each reestablish their own unique surface topography. As such, their fatigue lives differ at lower strain amplitudes, such as $\varepsilon_a = 0.003$ mm/mm (Fig. 7). The surface topographies after T process as shown in Fig. 6(e) reveal machining groves with a spacing of ~80 μm and a depth of ~3 μm. On the other hand, G and GDF produce shallower valleys (~1 μm) as shown in Figs. 6(c) and (d), respectively. This appears to be consistent with the observation in Fig. 7 that the shortest life registered for T specimens was shorter than those of the G and GDF specimens at lower strain levels such as $\varepsilon_a = 0.003$ mm/mm. The stress concentration is not only related to the depth of surface valley but also the radius of curvature at the root (Arola and Williams, 2002), as such both values should be considered to model fatigue lives. In addition, the fatigue notch factor most often does not equal the stress concentration factor. Depending on its ductility, a material's sensitivity to notches, and therefore, the fatigue notch factor may vary. Generally, brittle materials, which are more sensitive to notches, have fatigue notch factors approaching the stress concentration factor, and vice versa (Peterson, 1959). Further discussion regarding fatigue modeling using SR and geometrical factors will be followed in the fatigue modeling section.

It should be noted that surface treatments relying on mechanical material removal may introduce residual stresses, which tend to be compressive: Guo et al. (2010) showed that the residual stresses induced by T and G processes could enhance rolling contact fatigue performance. Jiang et al. (2006) found that the SB generated a thin layer of compressive residual stress which could result in increased fatigue life compared to untreated specimens although SR of SB parts are higher than untreated parts. Among the treatments considered in this work, T and SB can perhaps generate the most severe residual stresses, which likely have resulted in different levels of improvement in their fatigue lives. Specifically, SB specimens have evidently longer fatigue lives than the AB specimens, despite their similarly rough surface conditions. Besides, one of the T specimens at $\varepsilon_a = 0.003$ mm/mm has longer fatigue life compared to G specimens possibly because of the compressive residual stresses even though G specimens have substantially lower SR. Nevertheless, the effect of SR and geometrical factors on fatigue behavior still appear to be more significant compared to residual stresses in general. The measurement and considering the effect of residual stresses are beyond the scope of this work.

4.3. Fatigue modeling

The total strain-life curves, expressed in Eq. (3), based on Basquin equation for elastic deformation and Coffin-Manson equation for plastic deformation are generated using fatigue test results:

$$\frac{\Delta\varepsilon}{2} = \varepsilon_{\mathrm{a}} = \varepsilon_{\mathrm{ea}} + \varepsilon_{\mathrm{pa}} = \frac{\sigma'_f}{\mathrm{E}}(2\mathrm{N_f})^{\mathrm{b}} + \varepsilon'_f(2\mathrm{N_f})^{\mathrm{c}} \tag{3}$$

where σ'_f and b are fatigue strength coefficient and exponent, and ε'_f and c are fatigue ductility coefficient and exponent, respectively (Stephens et al., 2000). Based on Eq. (3), Fig. 13 presents the total strain-life curves (solid lines) with plastic and elastic strain-life curves (dashed and dash-dotted lines, respectively) with corresponding colors for the fatigue data from each surface condition. All constants for each surface condition are calculated and listed in Table 5. The constants for the GDF specimens ($\sigma'_f/E = 0.013$, $b = -0.099$, $\varepsilon'_f = 0.575$, and $c = -0.675$), as the best surface condition, are used as reference in further modeling.

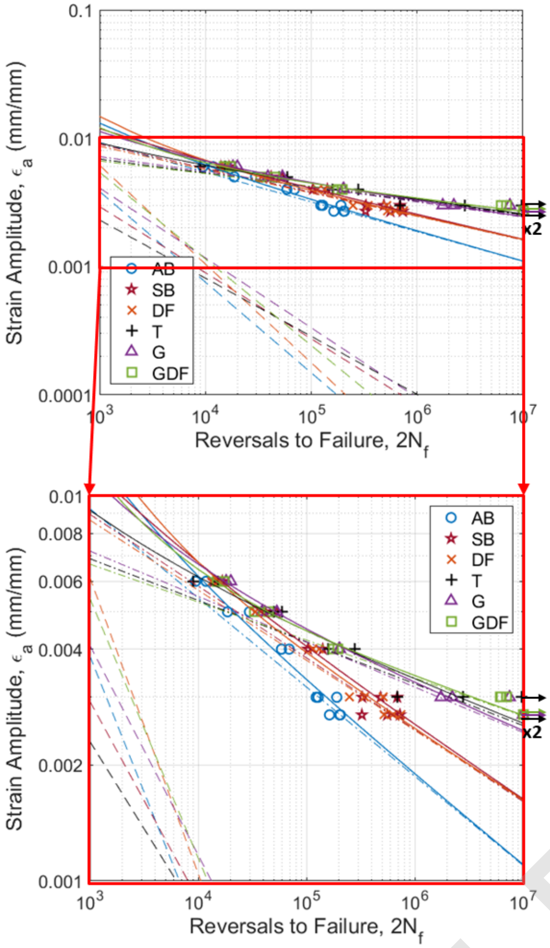

Fig. 13 Strain-life curves including elastic strain-life (dashed-dotted) and plastic strain-life (dashed) curves for each surface condition.

Table 5. Calculated σ'_f/E, b, ε'_f, and c for each surface condition.

Surface Condition	σ'_f/E	**b**	ε'_f	**c**
AB	0.046	-0.232	0.507	-0.707
SB	0.033	-0.187	0.103	-0.515
DF	0.030	-0.182	1.249	-0.769
T	0.015	-0.108	0.053	-0.453
G	0.016	-0.118	0.177	-0.545
GDF	0.013	-0.099	0.575	-0.675

To account for the effects of surface finish in strain-life behavior, the fatigue notch factor ($\overline{\mathrm{K}}_\mathrm{f}$) is calculated based on the notch sensitivity of the material ($\bar{\mathrm{q}}$), and the effective elastic stress concentration factor ($\overline{\mathrm{K}}_\mathrm{t}$) (Pegues et al., 2019). The expressions of $\bar{\mathrm{q}}$, $\overline{\mathrm{K}}_\mathrm{t}$, and $\overline{\mathrm{K}}_\mathrm{f}$ are given in Eqs. (4), (5), and (6), respectively:

$$\bar{\mathrm{q}} = 1/(1 + \frac{\gamma}{\bar{\rho}}) \tag{4}$$

$$\overline{\mathrm{K}}_\mathrm{t} = 1 + \mathrm{n}(\frac{\mathrm{R_v} + \mathrm{R_{mode}} \times \mathrm{R_{ku}} \times \mathrm{R_{sk}}}{\bar{\rho}}) \tag{5}$$

$$\overline{\mathrm{K}}_\mathrm{f} = 1 + \bar{\mathrm{q}}(\overline{\mathrm{K}}_\mathrm{t} - 1) \tag{6}$$

where γ is a material characteristic length, $\bar{\rho}$ is the effective radius of curvature and n is a stress state. γ is related to the grain size of the materials, which suggests that a decrease in the grain size can result in an increase in the notch sensitivity (Karry and Dolan, 1953). Therefore, the average grain size of the material (LB-PBF IN718, in this study) measured by electron backscatter diffraction analysis is used as the material characteristic length (γ = ~15 μm, in this study). The stress state, n, is assumed to be 2 for the tension (Arola and Williams, 2002). Since all specimens went through the same heat treatment and fully reversed compression-tension fatigue tests, γ and n are consistent regardless of surface conditions.

The effective radius of curvature can be different due to the surface treatments. Lee et al. (2021) showed that half of the layer thickness of AM parts can represent the effective radius of curvature in AB surfaces; therefore, the effective radius of curvature of AB specimens is considered as 20 μm ($\bar{\rho}$ = 20 μm). In addition, $\bar{\rho}$ of SB and DF specimens are also assumed as 20 μm since SB and DF, while mostly removed the peaks on the surface profile consisted of partially melted particles, they left some underlying surface topography constructed by the layer-by-layer process. It should be noted that measuring $\bar{\rho}$ based on line profiles is not valid for non-subtractive surface treatments because the line profile cannot fully represent 3D surface topography even if the length of the line profile is long enough. On the other hand, the specimens after subtractive methods (T and G) have different effective radii of curvature since the AB surface was completely removed by the machining processes. Based on polished longitudinal cross-sections of specimens, the average $\bar{\rho}$ of T and G are measured as 14 μm and 6 μm, respectively. Since hybrid SR parameters can be different depending on the measurement technique, the hybrid SR parameters obtained by the OM and XCT (automated method) are both utilized. Finally, the effective notch sensitivities, the effective elastic stress concentration factors, and the final effective fatigue notch factor for each surface condition are calculated and listed in Table 4 based on the obtained γ, $\bar{\rho}$, n, and hybrid SR parameter (i.e., $R_v+R_{mode}\times R_{sk}\times R_{ku}$).

Table 6 Calculated $\bar{q}$, $\bar{K}_t$, and $\bar{K}_f$ for each surface condition.

		OM (optical method)		**XCT (automated method)**	
Surface Condition	$\bar{q}$	$\bar{K}_t$	$\bar{K}_f$	$\bar{K}_t$	$\bar{K}_f$
AB	0.57	2.50	1.85	2.31	1.75
SB	0.57	1.98	1.56	2.02	1.58
DF	0.57	1.86	1.49	1.59	1.34
T	0.48	1.50	1.24	1.39	1.19
G	0.29	1.43	1.12	1.71	1.20

Estimation of fatigue lives of AB, SB, DF, T, and G specimens is attempted by applying their respective $\bar{K}_f$ as a reduction factor on the fatigue endurance limit of GDF specimens which are used as reference. In this study, the endurance limit is defined as the fatigue strength at 10^7 reversals. Only the elastic strain-life curve of GDF specimens is adjusted by $\bar{K}_f$ of each corresponded surface condition (Stephens et al., 2000). The estimated elastic strain-life curve is made as a straight line on the log-log plot connecting the elastic strain amplitude of GDF specimens at 2,000 reversals (ε_{ea} = 0.0062 mm/mm) and the reduced elastic strain amplitude at 10^7 reversals based on $\overline{\mathrm{K}}_\mathrm{f}$ for each surface condition. It is assumed that the plastic response for all surface conditions is similar since specimens have gone through the same heat treatment. Therefore, the plastic strain-life curve of GDF specimen (reference) is utilized for all conditions. Figures 14(a) and (c) show the total strain-life curves consisting of the plastic strain-life curve from the GDF specimens for all conditions and estimated elastic strain-life curves using $\overline{\mathrm{K}}_\mathrm{f}$ for each surface condition obtained by OM (optical method) and XCT (automated approach), respectively, which are overlaid by actual strain-life fatigue data points. The estimated versus experimental reversals to failure of all surface conditions using SR parameters calculated from OM and XCT measurements are also plotted in Figs. 14(b) and (d), respectively. The scatter bands of two and three are enclosed by blue dashed lines and red dashed-dotted lines, respectively.

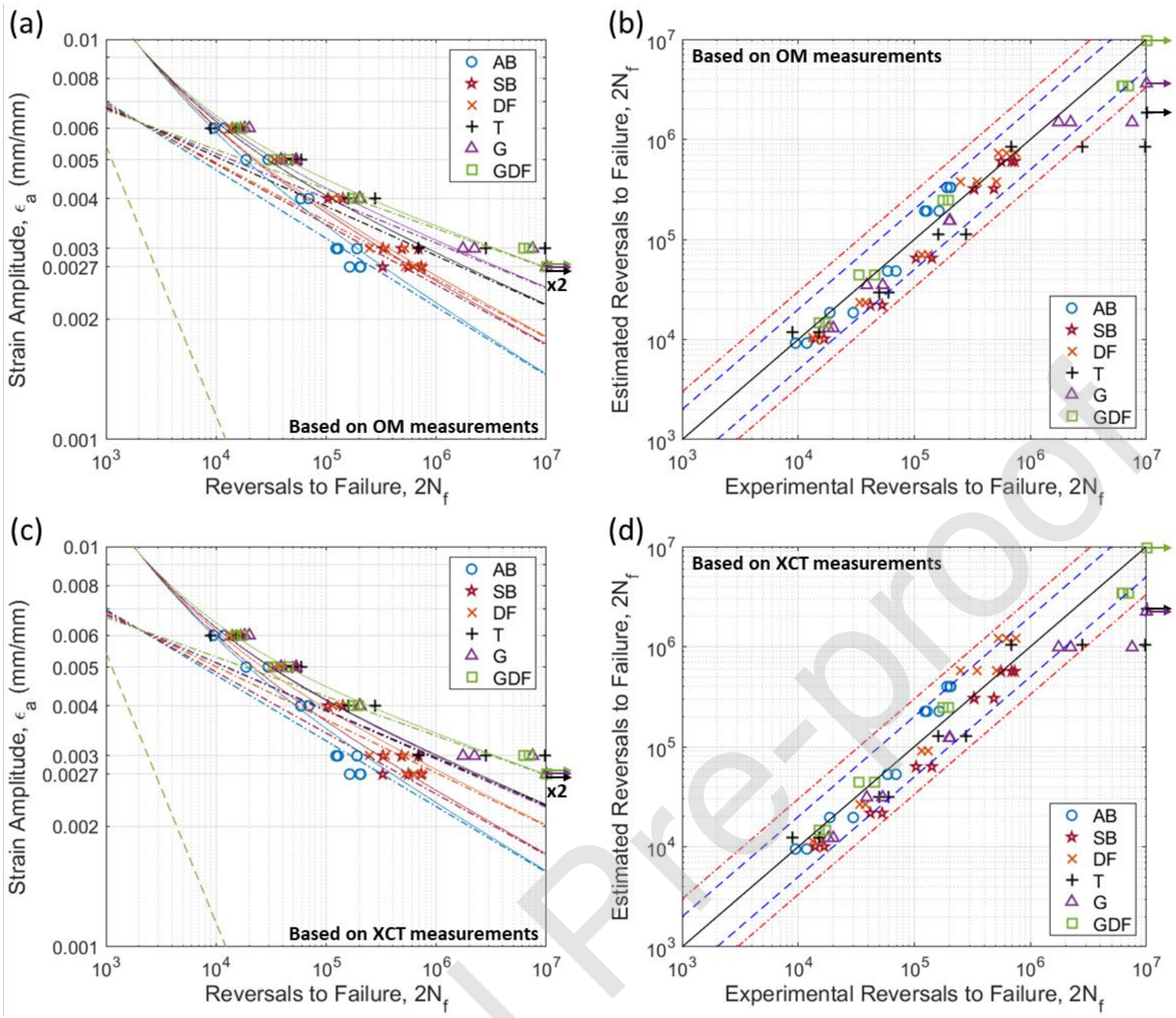

Fig. 14 Estimated total strain-life curves based on SR parameters measured by (a) OM and (c) XCT. Estimated versus experimental reversals to failure plots with scatter bands of two (blue dashed lines) and three (red dashed-dotted lines) using (b) OM and (d) XCT.

Without considering runouts, 95% and 89% of the estimated fatigue live based on OM measurements fall within the scatter bands of three and two, respectively, as shown in Fig. 14(b). In addition, 97% and 83% of estimations based on XCT measurements fall within the scatter bands of three and two from experimentally obtained fatigue lives, as shown in Fig. 14(d). Although there are a couple of data points falling outside of the scatter bands of three for each OM and XCT (Figs. 14(b) and (d), respectively) measured SR parameters, the estimated fatigue lives are less than experimentally obtained fatigue lives, which makes these estimations conservative. Therefore, SR measured by both OM and XCT can be used to estimate fatigue lives with reasonable accuracy using this effective notch factor model. It is evident from Figs. 14(b) and (d) that the predicted fatigue lives for T and SB conditions are predominantly underestimations. This observation is consistent with the prior argument made at the end of Section 4.2 that the compressive residual stress possible for these specimens might have beneficial effects.

5. Conclusions

This work investigated the effects of various surface treatments on the surface roughness —as measured by two techniques— and fatigue properties of laser beam powder bed fused IN718 specimens. The effect of surface treatment on the surface topography as well as SR metrics were assessed. The surface roughness values produced by different surface measurement techniques were also compared. Furthermore, fatigue modeling based on the effective fatigue notch factor approach and a hybrid surface roughness parameter was performed. Several conclusions can be drawn from this study:

1. Sand-blasting and drag-finishing were less aggressive in removing surface materials, only resulting in slight reduction in surface roughness and a moderate improvement in fatigue lives in the high cycle regime. In contrast, the subtractive treatments (including turning, grinding, and grinding + drag-finishing) more significantly improved the surface condition and fatigue performance.
2. While turning and grinding could substantially improve the surface condition, reflected by significantly reduced surface roughness metrics, the machining marks still provided sufficiently severe stress concentrations to induce crack initiation from the surface.

3. Both surface measurement techniques produced very comparable surface roughness values for all surface conditions except for the drag-finished specimens, for which the optical microscopy based technique was skewed by surface glaring and overestimated the surface roughness. The X-ray CT based technique appeared to be more reliable as it was capable of detecting near-surface AM defects and not subjected to the influence of surface glaring.
4. The effective fatigue notch factor model was demonstrated to satisfactorily correlate fatigue strain-life behavior with the hybrid surface roughness parameter obtained from both optical and X-ray CT based techniques. For all surface conditions, more than 95% and 83% of fatigue life estimations using the hybrid surface roughness parameter fell, respectively, within the scatter bands of three and two from experimentally obtained fatigue lives.

6. Disclaimer

Nima Shamsaei is the Guest Editor of this Special Issue on Additive Manufacturing. The editorial and peer-review process for this article was handled by the journal's Editor-in-Chief. Furthermore, the authors of this article do not have access to any confidential information related to its peer-review process.

Author statement

Seungjong Lee: Conceptualization, Methodology, Software, Validation, Formal analysis, Investigation, Data Curation, Writing- Original Draft, Visualization

Shuai Shao: Conceptualization, Methodology, Validation, Investigation, Formal analysis, Writing- Review & Editing, Visualization, Supervision

Douglas N. Wells: Conceptualization, Methodology, Validation, Resources, Writing- Review & Editing, Funding acquisition

Miroslav Zetek: Conceptualization, Methodology, Validation, Resources, Writing- Review & Editing, Funding acquisition

Miroslav Kepka: Conceptualization, Methodology, Validation, Resources, Writing- Review & Editing, Funding acquisition

Nima Shamsaei: Conceptualization, Methodology, Resources, Validation, Formal analysis, Investigation, Writing- Review & Editing, Supervision, Project administration, Funding acquisition

Acknowledgments

This material is based upon the work partially supported by the United States' National Aeronautics and Space Administration (NASA) under Award No. 80MSFC17M0023. Partial support from the United States' National Institute of Standards and Technology (NIST) under grant No. 70NANB18H220 is also acknowledged. The work was also partially supported by the Czech Republic's ERDF "Research of additive technologies for future applications in machinery industry - RTI plus" (No. CZ.02.1.01/0.0/0.0/18_069/0010040). Martin Bureš at the University of West Bohemia assisted with the post surface treatments.

References

AMS 5564, 2013. STEEL TUBING, CORROSION RESISTANT 19Cr - 10Ni (SAE 30304) High Pressure Hydraulic, Welded Plus Ultrasonically Tested or Seamless.

Arola, D., Williams, C.L., 2002. Estimating the fatigue stress concentration factor of machined surfaces. Int. J. Fatigue 24, 923–930. https://doi.org/10.1016/S0142-1123(02)00012-9

ASTM E606, 2021. ASTM E606 Standard Test Method for Strain-Controlled Fatigue Testing. ASTM Stand. https://doi.org/10.1520/E0606_E0606M-21

ASTM F3301, 2018. Standard for Additive Manufacturing – Post Processing Methods – Standard Specification for Thermal Post-Processing Metal Parts Made Via Powder Bed Fusion. ASTM Stand. 3. https://doi.org/10.1520/F3301-18A.2

Balachandramurthi, A.R., Moverare, J., Dixit, N., Pederson, R., 2018. Influence of defects and as-built surface roughness on fatigue properties of additively manufactured Alloy 718. Mater. Sci. Eng. A 735, 463–474. https://doi.org/10.1016/j.msea.2018.08.072

Barletta, M., Gisario, A., Venettacci, S., Rubino, G., 2014. A comparative evaluation of fluidized bed assisted drag finishing and centrifugal disk dry finishing. Eng. Sci. Technol. an Int. J. 17, 63–72. https://doi.org/10.1016/j.jestch.2014.03.007

Chan, K.S., 2015. Characterization and analysis of surface notches on Ti-alloy plates fabricated by additive manufacturing techniques. Surf. Topogr. Metrol. Prop. 3, 044006. https://doi.org/10.1088/2051-672X/3/4/044006

Frazier, W.E., 2014. Metal additive manufacturing: A review. J. Mater. Eng. Perform. https://doi.org/10.1007/s11665-014-0958-z

Gockel, J., Sheridan, L., Koerper, B., Whip, B., 2019. The influence of additive manufacturing processing parameters on surface roughness and fatigue life. Int. J. Fatigue 124, 380–388. https://doi.org/10.1016/j.ijfatigue.2019.03.025

Guo, Y.B., Warren, A.W., Hashimoto, F., 2010. The basic relationships between residual stress, white layer, and fatigue life of hard turned and ground surfaces in rolling contact. CIRP J. Manuf. Sci. Technol. 2, 129–134. https://doi.org/10.1016/j.cirpj.2009.12.002

Hamidi Nasab, M., Romano, S., Gastaldi, D., Beretta, S., Vedani, M., 2019. Combined effect of surface anomalies and volumetric defects on fatigue assessment of AlSi7Mg fabricated via laser powder bed fusion. Addit. Manuf. 34, 100918. https://doi.org/10.1016/j.addma.2019.100918

Hong, W., Lee, Y.T., Gong, H., 2005. A study of the staircase effect induced by material shrinkage in rapid prototyping. Rapid Prototyp. J. 11, 82–89. https://doi.org/10.1108/13552540510589449

Hosseini, E., Popovich, V.A., 2019. A review of mechanical properties of additively manufactured Inconel 718. Addit. Manuf. 30, 100877. https://doi.org/10.1016/j.addma.2019.100877

ISO 4287, 1997. ISO 4287:1997. Geometrical product specifications (GPS). Surface texture: profile method. Terms, definitions and surface texture parameters. ISO 4287.

Jia, Q., Gu, D., 2014. Selective laser melting additive manufacturing of Inconel 718 superalloy parts: Densification, microstructure and properties. J. Alloys Compd. 585, 713–721. https://doi.org/10.1016/j.jallcom.2013.09.171

Jiang, X.P., Wang, X.Y., Li, J.X., Li, D.Y., Man, C.S., Shepard, M.J., Zhai, T., 2006. Enhancement of fatigue and corrosion properties of pure Ti by sandblasting. Mater. Sci. Eng. A 429, 30–35. https://doi.org/10.1016/j.msea.2006.04.024

Johnson, A.S., Shao, S., Shamsaei, N., Thompson, S.M., Bian, L., 2017. Microstructure, Fatigue Behavior, and Failure Mechanisms of Direct Laser-Deposited Inconel 718. Jom 69, 597–603. https://doi.org/10.1007/s11837-016-2225-2

Kahlin, M., Ansell, H., Basu, D., Kerwin, A., Newton, L., Moverare, J.J., 2020. Improved fatigue strength of additively manufactured Ti6Al4V by surface post processing. Int. J. Fatigue 134, 105497. https://doi.org/10.1016/j.ijfatigue.2020.105497

Karry, R.W., Dolan, T.J., 1953. Influence of grain size on fatigue notch-sensitivity. ASTM Proc 53, 789–804.

King, W.E., Barth, H.D., Castillo, V.M., Gallegos, G.F., Gibbs, J.W., Hahn, D.E., Kamath, C., Rubenchik, A.M., 2014. Observation of keyhole-mode laser melting in laser powder-bed fusion additive manufacturing. J. Mater. Process. Technol. 214, 2915–2925. https://doi.org/10.1016/j.jmatprotec.2014.06.005

Kok, Y., Tan, X.P., Wang, P., Nai, M.L.S., Loh, N.H., Liu, E., Tor, S.B., 2018. Anisotropy and heterogeneity of microstructure and mechanical properties in metal additive manufacturing: A critical review. Mater. Des. https://doi.org/10.1016/j.matdes.2017.11.021

Krawczyk, B., Heine, B., Engelberg, D.L., 2016. Performance Optimization of Cold Rolled Type 316L Stainless Steel by Sand Blasting and Surface Linishing Treatment. J. Mater. Eng. Perform. 25, 884–893. https://doi.org/10.1007/s11665-016-1943-5

Leach, R.K., Giusca, C.L., Haitjema, H., Evans, C., Jiang, X., 2015. Calibration and verification of areal surface texture measuring instruments. CIRP Ann. - Manuf. Technol. 64, 797–813. https://doi.org/10.1016/j.cirp.2015.05.010

Lee, S., Pegues, J., Shamsaei, N., 2020. Fatigue Behavior and Modeling for Additive Manufactured 304L Stainless Steel: The effect of Surface Roughness. Int. J. Fatigue 141, 105856. https://doi.org/10.1016/j.ijfatigue.2020.105856

Lee, S., Rasoolian, B., Silva, D.F., Pegues, J.W., Shamsaei, N., 2021. Surface Roughness Parameter and Modeling for Fatigue Behavior of Additive Manufactured Parts: A Non-destructive Data-driven Approach. Addit. Manuf. 46, 102094. https://doi.org/10.1016/j.addma.2021.102094

Maleki, E., Bagherifard, S., Bandini, M., Guagliano, M., 2020. Surface post-treatments for metal additive manufacturing: Progress, challenges, and opportunities. Addit. Manuf. 37, 101619. https://doi.org/10.1016/j.addma.2020.101619

Muhammad, M., Frye, P., Simsiriwong, J., Shao, S., Shamsaei, N., 2021. An investigation into the effects of cyclic strain rate on the high cycle and very high cycle fatigue behaviors of wrought and additively manufactured Inconel 718. Int. J. Fatigue 144, 106038. https://doi.org/10.1016/j.ijfatigue.2020.106038

Pegues, J., Roach, M., Scott Williamson, R., Shamsaei, N., 2018. Surface roughness effects on the fatigue strength of additively manufactured Ti-6Al-4V. Int. J. Fatigue 116, 543–552. https://doi.org/10.1016/j.ijfatigue.2018.07.013

Pegues, J.W., Shamsaei, N., Roach, M.D., Williamson, R.S., 2019. Fatigue life estimation of additive manufactured parts in the as- built surface condition. Mater. Des. Process. Commun. 1, e36. https://doi.org/10.1002/mdp2.36

Peterson, R.E., 1959. Notch sensitivity. Met. fatigue 293–306.

Rahman, M., Seah, W.K.H., Teo, T.T., 1997. The machinability of Inconel 718. J. Mater. Process. Technol. 63, 199–204. https://doi.org/10.1016/S0924-0136(96)02624-6

Singh, S., Ramakrishna, S., 2017. Biomedical applications of additive manufacturing: Present and future. Curr. Opin. Biomed. Eng. 2, 105–115. https://doi.org/10.1016/j.cobme.2017.05.006

Stavroulakis, P.I., Leach, R.K., 2016. Invited Review Article: Review of post-process optical form metrology for industrial-grade metal additive manufactured parts. Rev. Sci. Instrum. 87, 1–15. https://doi.org/10.1063/1.4944983

Stephens, R.I., Fatemi, A., Stephens, R.R., Fuchs, H.O., 2000. Metal fatigue in engineering, 2nd ed. John Wiley & Sons.

Syam, W.P., Rybalcenko, K., Gaio, A., Crabtree, J., Leach, R.K., 2019. Methodology for the development of in-line optical surface measuring instruments with a case study for additive surface finishing. Opt. Lasers Eng. 121, 271–288. https://doi.org/10.1016/j.optlaseng.2019.04.015

Tang, M., Pistorius, P.C., Beuth, J.L., 2017. Prediction of lack-of-fusion porosity for powder bed fusion. Addit. Manuf. 14, 39–48. https://doi.org/10.1016/j.addma.2016.12.001

Townsend, A., Senin, N., Blunt, L., Leach, R.K., Taylor, J.S., 2016. Surface texture metrology for metal additive manufacturing: a review. Precis. Eng. 46, 34–47. https://doi.org/10.1016/j.precisioneng.2016.06.001

Tyagi, P., Goulet, T., Riso, C., Stephenson, R., Chuenprateep, N., Schlitzer, J., Benton, C., Garcia-Moreno, F., 2019. Reducing the roughness of internal surface of an additive manufacturing produced 316 steel component by chempolishing and electropolishing. Addit. Manuf. 25, 32–38. https://doi.org/10.1016/j.addma.2018.11.001

Wang, Z., Guan, K., Gao, M., Li, X., Chen, X., Zeng, X., 2012. The microstructure and mechanical properties of deposited-IN718 by selective laser melting. J. Alloys Compd. 513, 518–523. https://doi.org/10.1016/j.jallcom.2011.10.107

Xu, G.S., 2009. Sub-pixel edge detection based on curve fitting. 2009 2nd Int. Conf. Inf. Comput. Sci. ICIC 2009 2, 373–375. https://doi.org/10.1109/ICIC.2009.205

Yadollahi, A., Shamsaei, N., 2017. Additive manufacturing of fatigue resistant materials: Challenges and opportunities. Int. J. Fatigue 98, 14–31. https://doi.org/10.1016/j.ijfatigue.2017.01.001

Yin, Q., Liu, Z., Wang, B., Song, Q., Cai, Y., 2020. Recent progress of machinability and surface integrity for mechanical machining Inconel 718: a review. Int. J. Adv. Manuf. Technol. 109, 215–245. https://doi.org/10.1007/s00170-020-05665-4

Zhao, X., Rashid, A., Strondl, A., Hulme-Smith, C., Stenberg, N., Dadbakhsh, S., 2021. Role of Superficial Defects and Machining Depth in Tensile Properties of Electron Beam Melting (EBM) Made Inconel 718. J. Mater. Eng. Perform. 30, 2091–2101. https://doi.org/10.1007/s11665-021-05487-9